

Bilateral-Fuser: A Novel Multi-cue Fusion Architecture with Anatomical-aware Tokens for Fovea Localization

Sifan Song, Jinfeng Wang, Zilong Wang, Jionglong Su[†], Xiaowei Ding[†], Kang Dang[†]

Abstract—Accurate localization of fovea is one of the primary steps in analyzing retinal diseases since it helps prevent irreversible vision loss. Although current deep learning-based methods achieve better performance than traditional methods, there still remain challenges such as utilizing anatomical landmarks insufficiently, sensitivity to diseased retinal images and various image conditions. In this paper, we propose a novel transformer-based architecture (Bilateral-Fuser) for multi-cue fusion. This architecture explicitly incorporates long-range connections and global features using retina and vessel distributions for robust fovea localization. We introduce a spatial attention mechanism in the dual-stream encoder for extracting and fusing self-learned anatomical information. This design focuses more on features distributed along blood vessels and significantly decreases computational costs by reducing token numbers. Our comprehensive experiments show that the proposed architecture achieves state-of-the-art performance on two public and one large-scale private datasets. We also present that the Bilateral-Fuser is more robust on both normal and diseased retina images and has better generalization capacity in cross-dataset experiments.

Index Terms—Fovea Localization, Vision Transformer, Dual-Stream Architecture, Multi-Cue Fusion

I. INTRODUCTION

The fovea is anatomical landmark of the retina responsible for the most crucial part for sharp central vision at the center of the macula [1]. The detection of macula and fovea is an important prerequisite for the diagnosis of several retinal diseases, *e.g.*, diabetic maculopathy and age-related macular degeneration [2]–[4]. The severity of vision loss is often related to the distance between the fovea and associated abnormalities, such as hemorrhages and exudates [4].

Early detection of the location of the fovea is important to prevent the irreversible damage to vision [3], [5], [6]. The

location of fovea is often manually identified by clinicians, which is time consuming and laborious. Therefore, a robust and automated method of localizing the fovea center is essential. However, a number of challenges to fovea localization remain. First, the dark appearance of fovea is not distinguishable from the color intensity of the surrounding retinal tissue, and local anatomical landmarks (*e.g.*, blood vessels) are absent in the vicinity of the fovea [4], [7], [8]. Second, the accuracy in locating the fovea may be affected by the occurrence of retinal diseases [9]–[12]. For example, dark pathology caused by hemorrhages and microaneurysms may obscure the distinction between the fovea and retinal background. Some bright lesions, *e.g.*, exudates, may change the lightness of fovea to bright rather than dark, leading to erroneous localization results. Third, poor light conditions and non-standard fovea locations during photo shoot increase the difficulty of robust fovea localization [13]–[15]. Specifically, blurred and darkly illuminated photographs present challenges in estimating macula. For images where the optic disc (OD), rather than the macula, is centrally located, the symmetry may lead to predictions that are opposite to the ground-truth. Therefore, a robust fovea localization method is necessary to model features of the entire image at a global scale.

Fortunately, other anatomical structures outside the fovea, such as blood vessels, are useful for localization [2]–[4], [7]–[10], [12], [15]–[20]. Previous works generally use morphological methods to model the anatomical relationships between fovea and blood vessels [2]–[4], [9], [12]. However, these morphological methods may fail when the image has rare fovea position and color intensity as described above. In clinical diagnosis, fovea localization is an important upstream task that helps to diagnose maculopathy and abnormalities [2], [3]. While many recent works use deep learning methods to improve the performance, their input is only the fundus image [11], [13], [14], [21]–[25]. These works are also implemented on datasets containing few challenging images. As such, they have three main pitfalls: 1) The anatomical structure outside the macula are not exploited sufficiently since only fundus images are fed; 2) The typical convolution-based architectures lacks incorporation of global features; 3) The results of these works are sensitive to challenging cases, such as rare fovea positions and severe lesions.

To overcome these problems, we propose a novel architecture,

[†] Corresponding Authors.

This work was supported by the Key Program Special Fund in XJTU (KSF-A-22).

Sifan Song, Jinfeng Wang and Jionglong Su are with School of AI and Advanced Computing, XJTU Entrepreneur College (Taicang), Xi'an Jiaotong-Liverpool University, Suzhou, 215123, China (e-mail: {Sifan.Song19, Jinfeng.Wang20}@student.xjtlu.edu.cn, Jionglong.Su@xjtlu.edu.cn)

Zilong Wang and Kang Dang are with VoxelCloud, Inc., Los Angeles, California, 90024, USA (e-mail: {zlwang, kdang}@voxelcloud.net.cn)

Xiaowei Ding is with Shanghai Jiao Tong University, Shanghai, 200240, China (e-mail: dingxiaowei@sjtu.edu.cn)

Bilateral-Fuser, that is an updated version of our last work [15] (achieving best-paper-award finalist in *ISBI2022*). Inspired by TransFuser [26], we design a dual-stream encoder to fuse multi-cue features and a decoder to generate result maps. To utilize the anatomical structure outside the macula, the inputs of the encoder are images from two different cues (*i.e.*, fundus and vessel distribution). We then fuse the multi-cue features of fundus and vessel in four transformer-based modules (named Bilateral Token Incorporation, BTI) in the encoder. Thus global features and long-range connections are modeled for fovea localization, enabling robust performance even in challenging images. Unlike TransFuser, it directly reduces and recovers token numbers, applying average pooling and bilinear interpolation methods, respectively. Such operations may lead to information loss. We apply TokenLearner [27] in the BTI module. The attention mechanism of TokenLearner extracts self-learning spatial information from both cues. We illustrate that our design effectively exploits structural features along the optic disk and vessel distribution. Moreover, the attention mechanism reduces the number of tokens in the BTI module, thus significantly reducing the computational effort.

Our key contributions are as follows:

- We propose a novel dual-stream architecture for multi-cue fusion. Compared to typical convolutional-based fusion, this transformer-based structure globally incorporates long-range connections from multiple cues.
- We design the BTI module with learnable tokens for improving the efficiency of transformer-based fusion. Its adaptively learns tokens and to significantly reduce the token number from 1024 to 64. We visually demonstrate that, due to the spatial attention mechanism, the learnable tokens concentrates more on the feature along the vessel distribution for robust fovea localization.
- The proposed Bilateral-Fuser achieves state-of-the-art performance on three datasets (Messidor, PALM and Tisu) at only 0.25% computational cost (62.11G FLOPs) than the best previous work [15] (249.89G FLOPs). It also offers better performance and generalization capability in challenging cases.

II. RELATED WORK

A. Anatomical Structure-based Methods

Previous studies typically use traditional image processing techniques to estimate fovea regions, since the approximate location of macula is found anatomically correlated to the optic disk (OD) and blood vessels [2]–[4], [9], [10], [12], [28]. The fovea center is approximately on the symmetric line of main vessel branches through OD and is located approximately 2.5 OD diameters from the center of OD. These two features have been widely used for fovea localization [2], [4], [9], [10], [12], [28].

Some studies detect the fovea region based on OD location only. Narasimha *et al.* [10] propose a two-step approach incorporating the distance from OD center and the image

intensity so as to update the region of interest (ROI), and then locating the fovea center. Sekhar *et al.* [7] uses the spatial relationship to select a sector-shaped candidate ROI. The boundary of the sector is 30 degrees above and below the line through the center of the image and OD. Following this, they use a threshold to filter the intensity to estimate the fovea region. Blood vessels in color fundus images are relatively darker structures compared with OD. Some works utilize only extract the skeleton image of vessels to estimate ROI containing the macula. Deka *et al.* [3] and Medhi *et al.* [4] divide the image into several horizontal strips and select ROI with respect to the absence of blood vessels in the neighborhood of macula. Then they utilize thresholds to detect macula. Guo *et al.* [12] propose a morphological method to fit the segmented skeleton of major vessels using a parabola. The line of symmetry of the parabola is used to localize the fovea region.

Since the OD and vessels play a role in fovea localization, many existing studies utilize these two anatomical features. Asim *et al.* [8] estimate ROI dependent upon the pre-detected OD location and minimum intensity values, and then exclude the ROI near the vascular tree to improve the accuracy. Li *et al.* [9], Aquino *et al.* [2] and Fu *et al.* [28] also use a parabolic fit of major vessels to detect the orientation of the macula and use the anatomical relationship (*i.e.*, distance) between OD and fovea center to estimate the approximate location. The difference is that Fu *et al.* [28] use a deep learning method (U-Net [29]) rather the image processing method to detect OD and vessels. However, these methods based on anatomical features may underperform when processing pathological images. They also generally perform less competitively than more recent deep learning-based approaches.

Some attempts are made to localize macula with no anatomical features. For instance, GeethaRamani and Balasubramanian [11] propose an approach to segment macula by an unsupervised clustering algorithm. Pachade *et al.* [13] directly select the square in the middle of the image as ROI and use a filter on intensity for fovea localization. As they do not consider the anatomical features, such methods may fail when the illumination is different and the macula is not found in a standard location (*i.e.*, the center of the image).

B. Deep Neural Networks in Fovea Localization

Compared to traditional image processing and morphological techniques, deep learning has shown superiority in many fields of medical image analysis, such as classification, segmentation and object localization [30]–[34]. For the fovea localization task, existing studies can be categorized into two classes, namely, regression and segmentation.

Many deep learning-based methods formulate the fovea localization as a regression task. Al-Bander *et al.* [22] and Huang *et al.* [24] propose a two-step regression method that first predicts ROI and subsequently feeds the ROI into neural networks to localize the fovea center. Meyer *et al.* [23] and Bhatkalkar *et al.* [25] adopt pixel-wise distance/heatmap regression approaches for joint OD and fovea localization.

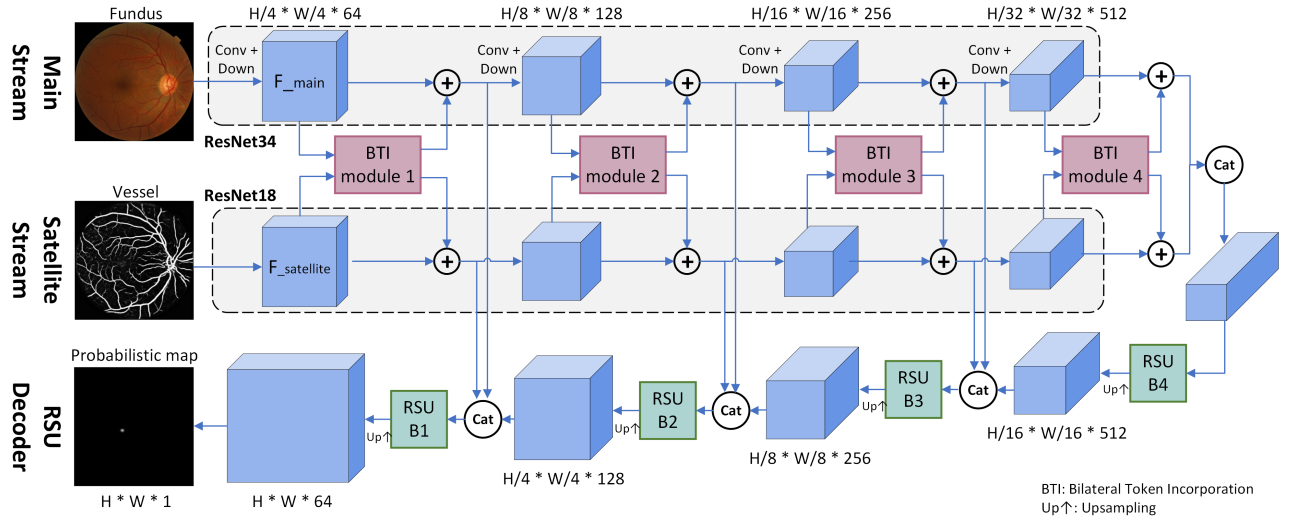


Fig. 1: The overall architecture of our proposed Bilateral-Fuser network.

Xie *et al.* [14] propose a hierarchical regression network that employs a self-attention mechanism in fovea localization [35], [36]. The network predicts the fovea center through a three-stage localization architecture crops features from coarse to fine.

Besides regression, image segmentation paradigm is also found in deep learning-based methods. Tan *et al.* [37] design a single 7-layer convolutional network to point-wise predict the fovea region from input image patches. Sedai *et al.* [21] propose a two-stage image segmentation framework for segmenting the fovea region from coarse to fine. However, standard CNN-based architectures have limited receptive fields due to fixed-size convolutional kernels, resulting in a lack of incorporation of long-range features. These CNN-based architectures may fail when light conditions and fovea positions are abnormal, or when information on OD and vessels is lacking due to lesions.

To address the issue of limited receptive field, our previous work models long-range connections by proposing a two-branch segmentation architecture (Bilateral-ViT [15]) utilizing a multi-head self-attention (MHSA) mechanism of transformer networks [38]–[40]. The main branch of Bilateral-ViT contains 12 consecutive MHSA layers in the bottleneck, constituting the global features for decoder. An additional vessel branch is designed to extract multi-scale spatial information from the vessel segmentation map as the second input. The decoder of Bilateral-ViT simultaneously fuses multi-cue features between fundus and blood vessel distribution, achieving the best reported results on two public datasets, Messidor [41] and PALM [42]. However, the multi-scale convolutional operation in the decoder has two main limitations, (1) non-global multi-cue feature fusion and (2) computationally expensive. To overcome these limitations, we propose a novel architecture Bilateral-Fuser, containing an encoder for global-connected multi-cue fusion and introduce adaptively learnable tokens to reduce computational amount.

III. METHODOLOGY

In this work, we propose a multi-cue fusion architecture, Bilateral-Fuser (Fig. 1), for robust fovea localization. The Bilateral-Fuser is based on a U-shape architecture whose encoder is a dual-stream structure, consisting of a main stream, a satellite stream and four intermediate Bilateral Token Incorporation (BTI) modules for exploiting and fusing global features from different cues. For the decoder, several ReSidual U-blocks (RSU) [32] are designed to effectively incorporate features from both main and satellite streams.

A. Overall Architecture

The overall architecture is given in Fig. 1. In the encoder, backbones of the main and satellite streams are ResNet34 and ResNet18, respectively. The main stream extracts detailed features from fundus images. The satellite stream extracts anatomical structure information from the distribution of blood vessels. Unlike the main stream whose input is a fundus image, a vessel segmentation map generated by a pre-trained model is fed into the satellite stream. The pre-trained vessel segmentation model is built on the DRIVE dataset [43] with the TransUNet [40] architecture, which is identical to [15].

The dual-stream encoder with four intermediate modules for multi-cue fusion is inspired by PVT [44] and TransFuser [26]. The backbone of each stream is split into four convolutional blocks, consisting of convolution and downsampling layers (Conv+Down). Subsequently, intermediate tensors (F_{main} and $F_{\text{satellite}}$) are fed into the BTI module which consists of a TokenLearner, T consecutive Multi-Head Self-Attention (MHSA) layers, and a TokenFuser. The BTI module fuses multi-cue features and encodes the long-range dependencies from fundus and vessel distribution. The output features are summed element-wise with skip-connected features and fed into the next convolution and downsampling layers. In addition, these output features from the BTI module are also passed to RSU blocks for later decoding operations.

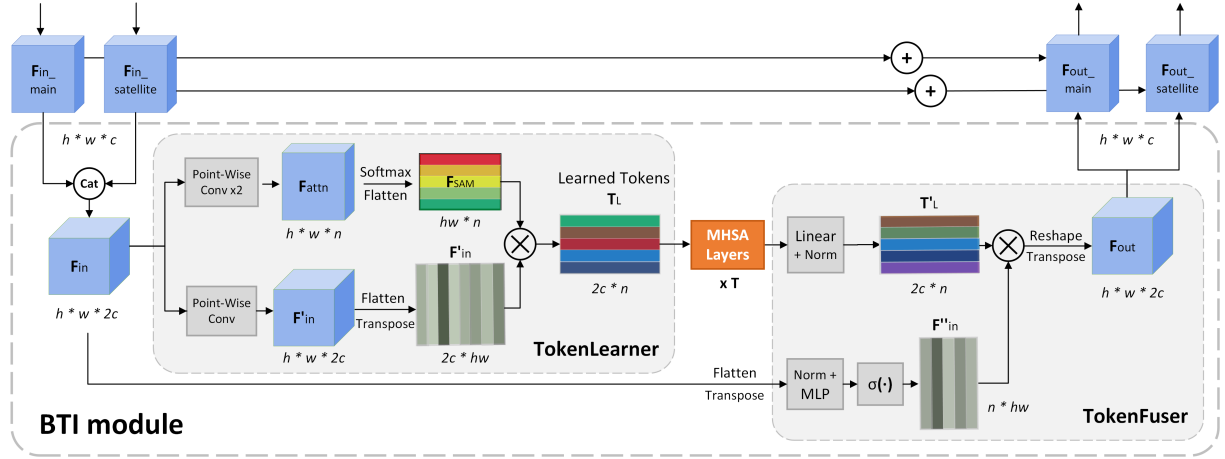


Fig. 2: The structure of BTI module used in our Bilateral-Fuser. It contains TokenLearner, $T \times$ MHSA layers and TokenFuser. The h , w and c are height, width, and channel of the corresponding input features. The n represents the number of learned tokens.

In contrast to the most commonly used plain convolutional blocks of the basic UNet decoder, four customized ReSidual U-blocks (RSU) [32] are utilized in the decoder of Bilateral-Fuser. The design is identical to our previous work [15] for effective multi-scale feature incorporation. As seen in Fig. 1, RSU B4 is the bottleneck between the encoder and decoder. The input to the other three RSU blocks is the concatenation of three types of features: (i) the multi-scale skip-connection features from the main stream, (ii) the multi-scale skip-connection features from the satellite stream, (iii) the hidden feature decoded by the previous RSU block. Qin *et al.* [32] report that the RSU block is superior in performance to other embedded structures (*e.g.*, plain convolution, residual-like, inception-like, and dense-like blocks), due to the enlarged receptive fields of the embedded U-shape architecture. The superiority of RSU structure as the decoder for incorporating multiple features has also been assessed by [15].

B. Bilateral Token Incorporation (BTI) modules

Standard transformer/MHSA-based architectures, such as Vision Transformer (ViT) [39] and TransUNet [40], typically split the input image into 2d windows (*e.g.*, 16×16 grid) to generate tokens. The tokenization output is then fed into subsequent MHSA layers for modeling long-range feature connectivity. However, those tokens are extracted individually from a fixed-size grid. Recent architectures with multiple transformer stages [26], [44] have several times more MHSA layers than the standard ViT. The naive tokens extracted by grids may contain uninformative or irrelevant features for visual understanding, which is computationally expensive.

To alleviate these pitfalls, the Bilateral Token Incorporation (BTI) module is designed for Bilateral-Fuser architecture (Fig. 2). We introduce the TokenLearner [27], which adaptively learns tokens through a spatial attention mechanism. After processed by MHSA layers (*head* = 8 and *layer* = 12 for each BTI module), the tokens are remapped by TokenFuser [27]

to the original dimensions as input tensor (Fig. 2). Thus, the benefits of the BTI module are (1) generating adaptive and learnable tokens to reduce token numbers, and (2) merging and fusing features with long-range dependencies of both cues with high efficacy.

1) TokenLearner: Let $\mathbf{F}_{in_main} \in \mathbb{R}^{h \times w \times c}$ and $\mathbf{F}_{in_satellite} \in \mathbb{R}^{h \times w \times c}$ be input tensors of the two streams, where h , w and c represent the height, width and channel of corresponding BTI module. As shown in Fig. 2, the concatenated feature $\mathbf{F}_{in} \in \mathbb{R}^{h \times w \times 2c}$ is first fed into TokenLearner. Customized from [27], we generate $\mathbf{F}_{attn} \in \mathbb{R}^{h \times w \times n}$ using two consecutive point-wise convolutional layers to reduce the dimensionality, where n is the number of learned tokens. After following the flatten and softmax functions, spatial attention maps with dimension $hw \times n$ are generated. Moreover, \mathbf{F}_{in} is processed by a point-wise convolutional layer, which is then flattened and transposed to become $\mathbf{F}'_{in} \in \mathbb{R}^{2c \times hw}$. To learn tokens adaptively by the spatial attention mechanism, the tokenization function is given by:

$$\mathbf{T}_L = \mathbf{F}'_{in} \mathbf{F}_{SAM} \quad (1)$$

$$\mathbf{F}_{SAM} = \text{softmax}(\text{flatten}(\mathbf{F}_{attn})) \quad (2)$$

where the learned tokens are $\mathbf{T}_L \in \mathbb{R}^{2c \times n}$. Because of the spatial attention mechanism, the learned tokens are modeled using informative combination of corresponding spatial locations. Compared to the 1024 tokens of ViT and TransUNet [39], [40], we retain only 8×8 tokens for each BTI module (for an input size of 512×512). Since the computation of MHSA is quadratic to the number of tokens, the computational cost is significantly decreased. Therefore, TokenLearner not only allows us to significantly reduce the number of tokens, but also to extract features related to the anatomical structure, *i.e.*, vessel distributions in this fovea localization task.

2) TokenFuser: As shown in Fig. 2, after the MHSA layers, the resulting tokens are recovered to the original tensor resolution ($h \times w \times 2c$) for further processing by Bilateral-Fuser.

So we first utilize a fully-connected (linear) layer for fusing information and then output $\mathbf{F}'_{\text{L}} \in \mathbb{R}^{2c \times n}$. By processing \mathbf{F}_{in} simultaneously, the output tensor \mathbf{F}_{out} is given by:

$$\mathbf{F}_{\text{out}} = (\mathbf{T}'_{\text{L}} \mathbf{F}_{\text{in}}'')^T \quad (3)$$

$$\mathbf{F}_{\text{in}}'' = \sigma(\text{MLP}(\text{flatten}(\mathbf{F}_{\text{in}})^T)) \quad (4)$$

where tensors $\mathbf{F}_{\text{in}}, \mathbf{F}_{\text{out}} \in \mathbb{R}^{h \times w \times 2c}$ and $\mathbf{F}_{\text{in}}'' \in \mathbb{R}^{n \times hw}$. $\sigma(\cdot)$ is a sigmoid function and MLP represents two dense layers with an intermediate GeLU activation function. In this case, the modeled tokens \mathbf{T}'_{L} are remapped to \mathbf{F}_{out} which has the original resolution of the initial \mathbf{F}_{in} . Following this, \mathbf{F}_{out} is equally split to $\mathbf{F}_{\text{out_main}}$ & $\mathbf{F}_{\text{out_satellite}}$ and added element-wise to the skip-connected features (*i.e.*, $\mathbf{F}_{\text{in_main}}$ & $\mathbf{F}_{\text{in_satellite}}$).

IV. EXPERIMENTS

A. Datasets and Network Configurations

We first perform experiments using the *Messidor* [41] and *PALM* [42] datasets. The *Messidor* dataset is developed for diabetic retinopathy analysis. It contain images of 540 normal and 660 diseased retinas. We utilize 1136 images from this dataset with fovea locations provided by [16]. The *PALM* dataset was released for the Pathologic Myopia Challenge (PALM) 2019. It consists of 400 images annotated with fovea locations, out of which 213 are pathologic myopia images, and 187 are normal retina images. For fairness of comparison, we keep our data split identically to [14] and [15].

We also use another large-scale dataset (4103 images, named *Tisu*) which is collected from our cooperating hospital. All data have been desensitized with patients personal information removed. This dataset is more challenging than the *Messidor* and *PALM* datasets, with a large number fundus images and containing many types of abnormalities, including hemorrhages, microaneurysms, and exudates. The ground-truth of fovea centers are averaged from the labels of three medical experts. For the purpose of training and testing, the images are split in a 4:1 ratio.

One of our main contributions is the significant reduction of FLOPs and GPU usage. Specifically, the proposed Bilateral-Fuser has approximately 0.25 times FLOPs, 0.48 times GPU training usage and 0.5 times GPU inference usage compared to the best previous work Bilateral-ViT [15]. To evaluate whether the performance of Bilateral-ViT is caused by its large computational amount, we design a light version, Bilateral-ViT/Lit (*i.e.*, Bi-ViT/Lit in Table I). The basic architecture of Bilateral-ViT is retained. We half of the middle channels of every convolutional blocks and reduce the token number of from 32×32 to 8×8 . In this case, the Bilateral-ViT/Lit has comparable FLOPs and GPU usage to our Bilateral-Fuser for more fair evaluations.

B. Implementation Details and Evaluation Metrics

We first remove the uninformative black background from the original fundus image, then pad and resize the cropped image

TABLE I: Configuration Comparison of Bilateral-ViT models and the proposed Bilateral-Fuser.

Methods	Tokens	Image Size	FLOPs	GPU/T ^a	GPU/I ^b
Bi-ViT [15]	32×32	512^2	249.89	16873	5459
Bi-ViT/Lit [15]	8×8	512^2	83.05	8653	3093
Bi-Fuser (Ours)	8×8	512^2	62.11	8083	2727

^a The GPU usage when training (MiB)

^b The GPU usage when inferencing (MiB)

region to a spatial resolution of 512×512 . We perform intensity normalization and data augmentation on the input images of the main branch and the vessel branch. To train our Bilateral-ViT network, we generate circular fovea segmentation masks from the ground-truth fovea coordinates. During the testing phase, we apply the sigmoid function to network prediction for the probabilistic map. We then collect all pixels and calculate their median coordinates as the final fovea location coordinates.

All experiments are coded using PyTorch and conducted on one NVIDIA GeForce RTX TITAN GPU. The optimizer used is Adam [45] and the batch size is 2. We employ a combination of dice loss and binary cross-entropy as the loss function. The configuration of the experiments performed on *Messidor* and *PALM* related to the Bilateral-ViT architectures is the same as in [15]. For our proposed Bilateral-Fuser, the initial learning rate is $1e^{-3}$, which gradually decays to $1e^{-9}$ over 300 epochs using the CosineAnnealingLR strategy on *Messidor* and *PALM*. For the large-scale dataset *Tisu*, the initial learning rate is altered to $6e^{-5}$ for all experiments.

To evaluate the performance of fovea localization, we adopt the following evaluation protocol [14]–[16], [23]: the fovea localization is considered successful when the Euclidean distance between the ground-truth and predicted fovea coordinates is no larger than a predefined threshold value, such as the optic disc radius R . For a comprehensive evaluation, accuracy corresponding to different evaluation thresholds (for example, $2R$ indicating the predefined threshold values are set to twice the optic disc radius R) is usually reported.

V. RESULTS

A. Comparison to State of the Art

In Table II, we compare the performance of Bilateral-Fuser to existing methods on both public dataset, *Messidor* and *PALM*. We classify all methods in Table II according to whether they use deep learning techniques and whether multi-cue features are used. We observe that the traditional morphological methods [2], [16]–[20] utilize anatomical landmarks (vessels or OD) outside the macula. Bilateral-ViT [15] is the only previous deep learning-based architecture that incorporates fundus and vessel features. However, in most deep learning-based studies [11], [13], [14], [22]–[25], only fundus images are used, resulting in poor incorporation of anatomical relationships throughout the entire image, leading to failure in the more challenging cases.

With the advantages of the transformer-based multi-cue fusion encoder and adaptive learning tokens, our proposed

TABLE II: Comparison with existing studies using the Messidor and PALM datasets based on the R rule. The best and second best results are highlighted in bold and italics respectively.

Messidor	DL ^a	MF ^b	1/4 R (%)	1/2 R (%)	1R (%)	2R (%)
Gegundez-Arias <i>et al.</i> (2013) [16]	✗	✓	76.32	93.84	98.24	99.30
Giachetti <i>et al.</i> (2013) [17]	✗	✓	-	-	99.10	-
Aquino (2014) [2]	✗	✓	83.01	91.28	98.24	99.56
Dashtbozorg <i>et al.</i> (2016) [18]	✗	✓	66.50	93.75	98.87	99.58
Girard <i>et al.</i> (2016) [19]	✗	✓	-	94.00	98.00	-
Molina-Casado <i>et al.</i> (2017) [20]	✗	✓	-	96.08	98.58	99.50
Al-Bander <i>et al.</i> (2018) [22]	✓	✗	66.80	91.40	96.60	99.50
Meyer <i>et al.</i> (2018) [23]	✓	✗	94.01	97.71	99.74	-
GeethaRamani <i>et al.</i> (2018) [11]	✓	✗	85.00	94.08	99.33	-
Pachade <i>et al.</i> (2019) [13]	✓	✗	-	-	98.66	-
Huang <i>et al.</i> (2020) [24]	✓	✗	70.10	89.20	99.25	-
Xie <i>et al.</i> (2020) [14]	✓	✗	98.15	99.74	99.82	100.00
Bhatkalkar <i>et al.</i> (2021) [25]	✓	✗	95.33	99.74	100.00	-
Bi-ViT (2022) [15]	✓	✓	98.59	100.00	100.00	100.00
Bi-ViT/Lit (2022) [15]	✓	✓	98.50	100.00	100.00	100.00
Bi-Fuser (Ours)	✓	✓	98.86	100.00	100.00	100.00
PALM	DL ^a	MF ^b	1/4 R (%)	1/2 R (%)	1R (%)	2R (%)
Xie <i>et al.</i> (2020) [14]	✓	✗	-	-	94	-
Bi-ViT (2022) [15]	✓	✓	65	83	96	98
Bi-ViT/Lit (2022) [15]	✓	✓	55	80	94	96
Bi-Fuser (Ours)	✓	✓	69	85	97	98

^a Whether the method is based on deep learning (DL).

^b Whether the method is based on multi-cue features (MF), *e.g.*, fundus images, vessels or optical discs.

TABLE III: Comparison of performance on normal and diseased retinal images using the Messidor and PALM datasets. The best and second best results are highlighted in bold and italics respectively.

Messidor	MF ^a	FLOPs _↓	Err _↓	1/4 R(%)		1/2 R(%)		1R(%)		2R(%)	
				Normal	Diseased	Normal	Diseased	Normal	Diseased	Normal	Diseased
UNet (2015) [29]	✗	193.31	12.39	95.15	93.33	97.76	95.00	97.95	95.33	97.95	95.33
U2 Net (2020) [32]	✗	151.00	7.31	98.51	97.33	99.63	99.50	99.63	99.50	99.63	99.50
TransUNet (2021) [40]	✗	168.73	7.61	98.32	97.67	100.00	99.83	100.00	99.83	100.00	99.83
Bi-ViT (2022) [15]	✓	249.89	6.81	98.51	98.67	100.00	100.00	100.00	100.00	100.00	100.00
Bi-ViT/Lit (2022) [15]	✓	83.05	6.77	98.69	98.33	100.00	100.00	100.00	100.00	100.00	100.00
Bi-Fuser (Ours)	✓	62.11	6.77	99.07	98.67	100.00	100.00	100.00	100.00	100.00	100.00
PALM	MF ^a	FLOPs _↓	Err _↓	1/4 R(%)		1/2 R(%)		1R(%)		2R(%)	
				Normal	Diseased	Normal	Diseased	Normal	Diseased	Normal	Diseased
UNet (2015) [29]	✗	193.31	149.30	74.47	18.87	76.60	41.51	76.60	64.15	78.72	73.58
U2 Net (2020) [32]	✗	151.00	62.62	93.62	28.30	95.74	60.38	97.87	84.91	97.87	98.11
TransUNet (2021) [40]	✗	168.73	104.38	95.74	18.87	97.87	43.40	97.87	75.47	97.87	84.91
Bi-ViT (2022) [15]	✓	249.89	53.70	95.74	37.74	97.87	69.81	100.00	92.45	100.00	96.23
Bi-ViT/Lit (2022) [15]	✓	83.05	62.47	87.23	26.42	93.62	67.92	97.87	90.57	97.87	94.34
Bi-Fuser (Ours)	✓	62.11	48.72	95.74	45.28	97.87	73.58	100.00	94.34	100.00	96.23

^a Whether the method is based on multi-cue features (MF), *e.g.*, fundus images, vessels or optical discs.

Bilateral-Fuser achieves the best performance in all evaluation settings of Messidor and PALM compared to all previous studies. In Table II, on the Messidor dataset, Bilateral-Fuser achieves the best accuracy of 98.86% at 1/4R, with gains of 0.71% and 3.53% compared to the previous works [14] and [25], respectively. Our network also achieves a slightly better performance than Bilateral-ViT [15] and its light version. The proposed Bilateral-Fuser achieves 100% accuracy at the evaluation thresholds of 1/2R, 1R, and 2R; in other words, the localization error is at most 1/2R (approximately 19 pixels for an input image size of 512 × 512).

PALM is a more challenging dataset with fewer images and complex diseased patterns. In Table II, our method demonstrates

its superiority over all other methods from 1/4R to 2R. It achieves accuracies of 69% and 85% at 1/4R and 1/2R, which are 4% and 2% better than Bilateral-ViT, respectively. In addition, it achieves 14% improvement (1/4R) over Bilateral-ViT/Lit, and 3% improvement (1R) over both Bilateral-ViT/Lit and [14]. Therefore, our Bilateral-Fuser achieves state-of-the-art performance on both Messidor and PALM datasets with high computational efficiency.

B. Fovea Localization on Normal and Diseased Images

According to normal and diseased cases in Messidor and PALM, the performance is separately demonstrated to assess

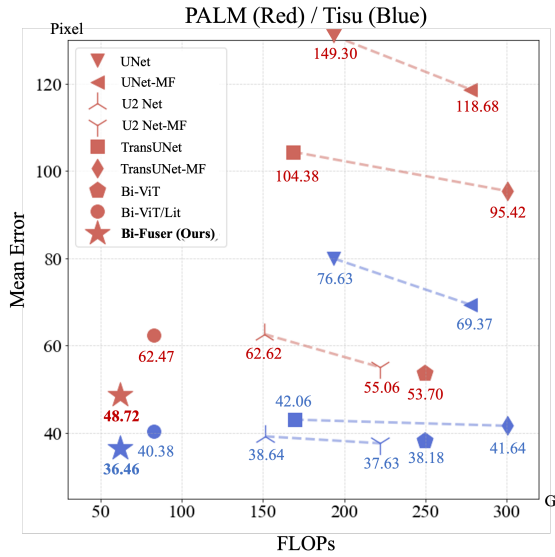


Fig. 3: Visualization of mean errors (Y-axis) of different multi-cue fusion models. X-axis is the computational cost (FLOPs). The red and blue markers are results on PALM and Tisu datasets, respectively. Numbers below the markers are corresponding mean errors.

the robustness of fovea localization (Table III). We implement several widely used segmentation networks as comparison baselines, *e.g.*, UNet [29], U2 Net [32], and a hybrid version of TransUNet with ResNet50 for patch embedding [40]. The models of Bilateral-ViT, Bilateral-ViT/Lit and our Bilateral-Fuser are identical to those used in Table II.

In Table III, our Bilateral-Fuser achieves the smallest error (Err) with the smallest computational cost (FLOPs) on both datasets. Bilateral-ViT [15] and our proposed Bilateral-Fuser both obtains 100% accuracy from $1/2R$ to $2R$ on all the Messidor images, and 100% accuracy of $1R$ and $2R$ on normal PALM images. Compared to existing methods, Bilateral-Fuser demonstrates its superior performance on almost all metrics on Messidor. Although Bilateral-Fuser has only 0.25 times FLOPs (62.11G) to Bilateral-ViT (249.89G), it achieves the best performance on diseased images of PALM from $1/4R$ to $2R$, with up to 7.54% improvement compared to the other methods ($1/4R$, Diseased). Its improvement is significantly increased to 18.86% ($1/4R$, Diseased) compared to Bilateral-ViT/Lit (83.05G, *i.e.*, the network with the closest FLOPs to Bilateral-Fuser). Thus, this suggests that the performance of Bilateral-Fuser is highly reliable on both normal and diseased fundus images with high efficacy.

C. Comparison of Multi-Cue Fusion Architectures

To comprehensively assess the performance of models with input features in multiple cues (fundus and vessel distributions), we implement a multi-cue fusion version for the baseline models, UNet, U2 Net and TransUNet. We utilize two identical encoders with inputs of a fundus image and a vessel map. The features are extracted independently and then concatenated at

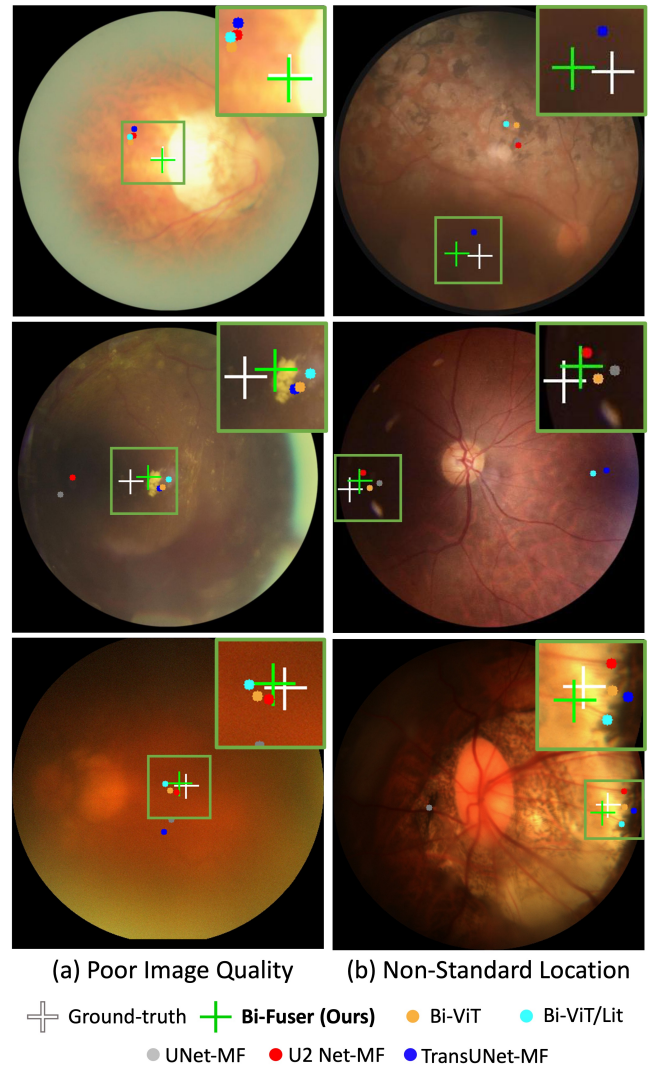


Fig. 4: Visual results of fovea localization predicted by different methods.

the bottleneck for decoding (similar to [26], [46]). The modified baseline models are named as UNet-MF, U2 Net-MF and TransUNet-MF. Table III also suggests that architectures using multi-cue features outperform typical networks with fundus-only input. This comparison in PALM is more apparent because PALM contains more challenging images than Messidor. Compared to PALM images, the Tisu images are not only larger in number (400 vs. 4103) but also contain more disease types with varying degree of severity. Therefore, the results on PALM and Tisu dataset demonstrate the potential of architectures in handling complex datasets.

Fig. 3 shows the performance comparison of the described architectures (mean error against FLOPs) on PALM (red markers) and Tisu (blue markers). In Fig. 3, numbers below the markers are mean errors and the dashed lines connect each standard baseline model and its multi-cue fusion architecture (MF). These multi-cue fusion versions (UNet-MF, U2 Net-MF and TransUNet-MF) outperform their standard versions at a considerably higher computational cost due to the additional

TABLE IV: The performance of cross-dataset experiments. The models used here are exactly those selected in Fig. 3 (blue markers). **Top** and **Bottom:** The models trained on Tisu and tested on PALM and Messidor, respectively. The best and second best results are highlighted in bold and italics respectively.

Tisu→Messidor	Err _↓	1/4 R (%)	1/2 R (%)	1R (%)	2R (%)
UNet-MF (2015) [29]	8.89	97.45	99.38	99.65	99.65
U2 Net-MF (2020) [32]	8.48	97.10	99.91	100.00	100.00
TransUNet-MF (2021) [40]	8.25	97.45	99.82	100.00	100.00
Bi-ViT (2022) [15]	7.30	98.59	100.00	100.00	100.00
Bi-ViT/Lit (2022) [15]	7.37	98.06	99.91	100.00	100.00
Bi-Fuser (Ours)	7.62	98.59	99.91	100.00	100.00
Tisu→PALM	Err _↓	1/4 R (%)	1/2 R (%)	1R (%)	2R (%)
UNet-MF (2015)	137.14	52.25	64.25	77.25	85.50
U2 Net-MF (2020)	69.46	55.00	73.25	90.00	97.25
TransUNet-MF (2021)	78.98	53.50	71.75	87.50	95.75
Bi-ViT (2022) [15]	64.73	56.00	72.75	90.00	97.75
Bi-ViT/Lit (2022) [15]	71.14	55.50	73.25	90.75	97.00
Bi-Fuser (Ours)	59.21	55.25	73.25	93.50	98.50

encoder. In Fig. 3, we can see that the performance comparison (MF versions vs. baseline models) is more apparent on PLAM since the dataset size of PLAM is much smaller than Tisu (400 vs. 4103). For all multi-cue fusion architectures, the proposed Bilateral-Fuser achieves the best results (smallest errors) on both PLAM (48.72 pixels) and Tisu (36.46 pixels). It requires only 62.11G FLOPs which is four times less than Bilateral-ViT (249.89G). Compared to the model with comparable FLOPs (Bilateral-ViT/Lit, 83.05G), Bilateral-Fuser shows significant advantages of 13.75 and 3.92 on PLAM and Tisu, respectively.

Fig. 4 provides some visual results of fovea localization on severe disease images from the PALM and Tisu datasets. These images in Fig. 4-a and Fig. 4-b are also affected by poor image quality and non-standard fovea locations, respectively. Our Bilateral-Fuser generates the most accurate predictions for a number of difficult cases with poor lighting conditions and blurred appearance (Fig. 4-a). For another challenging types (Fig. 4-b), where the macula is close to the image boundary, predictions of Bilateral-Fuser (green crosses) are also closest to the ground-truth (white crosses). In contrast, the fovea locations predicted by other architectures that cannot globally incorporate long-range multi-cue features may appear on the wrong side of the optic disc (Fig. 4-b). These results suggest that the architecture of Bilateral-Fuser can adequately model fundus and vessel features of two streams, resulting in superior performance to other networks.

D. Performance of Cross-Dataset Experiments

We conduct cross-dataset experiments to assess the generalization capability of the proposed Bilateral-Fuser. In Table IV, the models trained on Tisu (exactly the same ones in Fig. 3) are used to test on Messidor and PALM datasets. In Table IV-**Top**, our Bilateral-Fuser generally achieves similar accuracies as the other results from 1/4R to 2R on Messidor. For the more difficult dataset PALM, Bilateral-Fuser achieves an improvement of 5.52 and 11.93 pixels in the average localization error at the original image resolution compared to Bilateral-ViT (64.73 pixels) and its lighter version (71.14 pixels), respectively

TABLE V: Comparison of performance between different inputs for the main and satellite streams on PALM and Tisu datasets. The best and second best results are highlighted in bold and italics.

PALM	Err _↓	1/4 R (%)	1/2 R (%)	1R (%)	2R (%)
Fundus+Vessel (Ours)	48.72	69	85	97	98
Fundus-only	54.46	64	85	95	98
Vessel-only	72.25	57	75	92	97
Tisu	Err _↓	1/4 R (%)	1/2 R (%)	1R (%)	2R (%)
Fundus+Vessel (Ours)	36.46	52.32	75.49	92.93	97.44
Fundus-only	37.48	52.32	73.78	91.10	96.95
Vessel-only	48.13	33.66	61.83	89.39	96.83

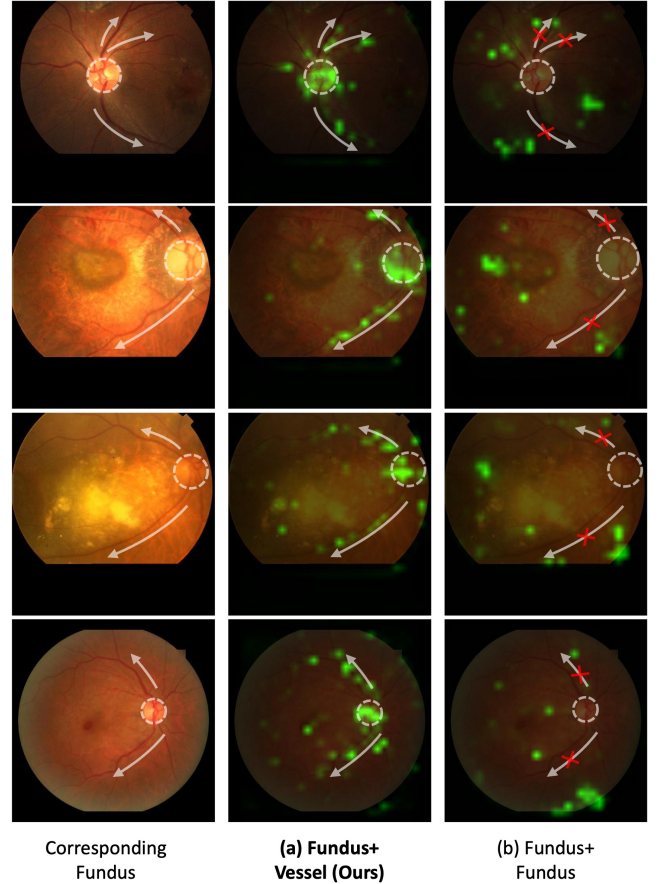


Fig. 5: Visualizations generated from spatial attention maps, indicating the focus of TokenLearner in BTI module. These visual results have been resized and superimposed onto the corresponding fundus.

(Table IV-**Bottom**). In addition, the proposed Bilateral-Fuser outperforms the baselines (multi-cue fusion version) by a significant margin (at least 10.25 pixels), demonstrating its excellent generalization capability and robustness.

E. Ablation Study

1) *Comparison of Inputs for Bilateral-Fuser:* In Table V, we compare the experiment performance of Bilateral-Fuser using different inputs. In the standard setup (Fundus+Vessel), we select fundus images and vessel maps as inputs for the main stream and satellite stream, respectively. These experiments achieve the best accuracy on all metrics, with the smallest

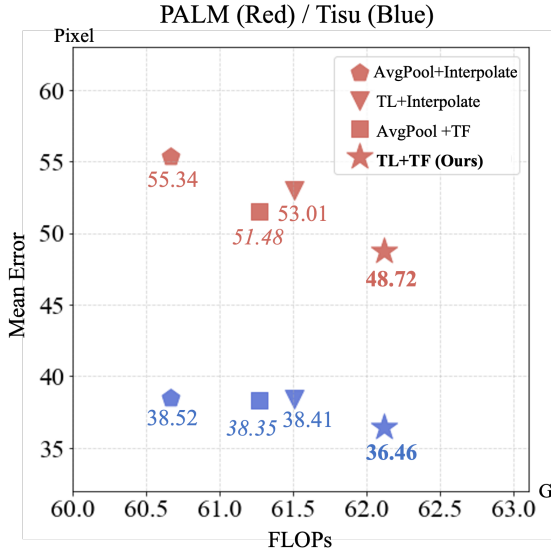


Fig. 6: Visualization of mean errors (Y -axis) of ablation studies for reducing and recovering tokens. X -axis is the computational cost (FLOPs). The red and blue markers are results on PALM and Tisu datasets, respectively. Numbers below the markers are corresponding mean errors.

mean error on PALM (48.72 pixels) and Tisu (36.46 pixels). Table V demonstrates the results using fundus as the second input (Fundus+Fundus). Although fundus images contain more detailed information than vessel maps, feeding them into the satellite stream does not provide anatomical structure to guide TokenLearner. In this case, TokenLearner may not learn to focus its attention on the more useful anatomical features, leading to a slight performance degradation. Then, experiments using vessel maps as both inputs (Vessel+Vessel) are also conducted, but their accuracies decrease significantly on both PALM and Tisu by 23.53 and 11.67 pixels, respectively. Such results suggest that having only vessel maps as inputs to both streams leads to a severe loss of information.

Since the spatial attention maps reveal features of self-learning extracted by TokenLearners, we visually demonstrate these weight maps in Fig. 5. We maximize the probability values along the channels of spatial attention maps, and then normalize them to visualize the attention of tokens in element-wise. These maps are resized and superimposed onto the corresponding fundus to compare their structural relationships.

We observe that our Fundus+Vessel experiments focus on wide-ranging structural features along the optic disk and the direction of vessel branches (Fig. 5-a). This is feasible since these two structures have significant anatomical relationships with the fovea region [2], [7]–[10]. In contrast, although more detailed information is available to the Fundus+Fundus experiments, these TokenLearners, which are not guided by anatomical structures, fail to learn features along the vessel distribution (Fig. 5-b). Since fewer tokens carry useful features related to fovea localization, the intermediate BTI modules may have restricted effects in Bilateral-Fuser, leading to slight

underperformance on PALM and Tisu datasets (Table V).

2) Comparison of Methods for Reducing and Recovering Tokens: We conduct a comprehensive set of ablation experiments to assess the effectiveness of different components in reducing and recovering token numbers on PALM and Tisu datasets. Instead of using TokenLearner (TL) and TokenFuser (TF) with adaptively learnable parameters, we alternatively test more straightforward methods used in [26], average pooling (AvgPool) and bilinear interpolation (Interpolate), respectively.

In Fig. 6, we demonstrate the visualization of the mean error in relation to the computational cost (FLOPs) on PALM (red) and Tisu (blue). Compared to other configurations, experiments using both TokenLearner and TokenFuser (TL+TF) achieve the best performance on PALM and Tisu (mean error of 48.72 and 36.46 pixels), respectively. This may be due to the loss of information caused by the direct reduction and recovery of token numbers (*i.e.*, AvgPool and Interpolate). In the proposed Bilateral-Fuser (TL+TF), total excess costs of FLOPs for four BTI modules utilizing TokenLearner and TokenFuser are only **0.85G** and **0.61G**, respectively. Such a slight increase in computation leverages a significant performance benefit. Therefore, the adaptively learnable parameters of TokenLearner and TokenFuser in our Bilateral-Fuser improve the performance with high efficacy on PALM and Tisu.

VI. CONCLUSIONS

Accurate detection of the macula and fovea is important in diagnosing retinal diseases. While anatomical structures outside the fovea, such as the blood vessel distribution, are anatomically related to the fovea, relatively few recent deep learning approaches exploit them to improve the performance of fovea localization. In this paper, we propose a novel architecture, Bilateral-Fuser, which fuses features on the retina and corresponding vessel distribution with high efficacy for robust fovea localization. The Bilateral-Fuser contains a two-stream encoder for multi-cue fusion and a decoder for generating result maps. In addition, the Bilateral Token Incorporation (BTI) module in the encoder is designed to incorporate global anatomical features of inputs (both fundus and vessel images). Comprehensive experiments carried out demonstrate that the advantages of using Bilateral-Fuser with are more accurate localization results, insensitivity to diseased images, and low computational cost. Our proposed architecture achieves new state-of-the-art on two public datasets (Messidor and PALM) and one large-scale private dataset (Tisu) with metrics from $1/4 R$ to $2R$. It also outperforms other methods on cross-dataset experiments with better generalization capacity.

REFERENCES

- [1] J. Weiter, G. Wing, C. Trempe, and M. Mainster, “Visual acuity related to retinal distance from the fovea in macular disease.” *Annals of ophthalmology*, 1984.
- [2] A. Aquino, “Establishing the macular grading grid by means of fovea centre detection using anatomical-based and visual-based features,” *Computers in biology and medicine*, 2014.

- [3] D. Deka, J. P. Medhi, and S. Nirmala, "Detection of macula and fovea for disease analysis in color fundus images," in *International Conference on Recent Trends in Information Systems (ReTIS)*, 2015.
- [4] J. P. Medhi and S. Dandapat, "An effective fovea detection and automatic assessment of diabetic maculopathy in color fundus images," *Computers in biology and medicine*, 2016.
- [5] K. S. Deepak and J. Sivaswamy, "Automatic assessment of macular edema from color retinal images," *IEEE Transactions on medical imaging*, vol. 31, no. 3, pp. 766–776, 2011.
- [6] L. Giancardo, F. Meriaudeau, T. P. Karnowski, Y. Li, S. Garg, K. W. Tobin Jr, and E. Chaum, "Exudate-based diabetic macular edema detection in fundus images using publicly available datasets," *Medical image analysis*, vol. 16, no. 1, pp. 216–226, 2012.
- [7] S. Sekhar, W. Al-Nuaimy, and A. K. Nandi, "Automated localisation of optic disk and fovea in retinal fundus images," in *2008 16th European Signal Processing Conference*, 2008.
- [8] K. M. Asim, A. Basit, and A. Jalil, "Detection and localization of fovea in human retinal fundus images," in *2012 International Conference on Emerging Technologies*, 2012.
- [9] H. Li and O. Chutatape, "Automated feature extraction in color retinal images by a model based approach," *IEEE Transactions on biomedical engineering*, 2004.
- [10] H. Narasimha-Iyer, A. Can, B. Roysam, V. Stewart, H. L. Tanenbaum, A. Majerovics, and H. Singh, "Robust detection and classification of longitudinal changes in color retinal fundus images for monitoring diabetic retinopathy," *IEEE transactions on biomedical engineering*, 2006.
- [11] R. GeethaRamani and L. Balasubramanian, "Macula segmentation and fovea localization employing image processing and heuristic based clustering for automated retinal screening," *Computer methods and programs in biomedicine*, 2018.
- [12] X. Guo, H. Wang, X. Lu, X. Hu, S. Che, and Y. Lu, "Robust fovea localization based on symmetry measure," *IEEE Journal of Biomedical and Health Informatics*, vol. 24, no. 8, pp. 2315–2326, 2020.
- [13] S. Pachade, P. Porwal, and M. Kokare, "A novel method to detect fovea from color fundus images," in *Computing, Communication and Signal Processing*. Springer, 2019.
- [14] R. Xie, J. Liu, R. Cao, C. S. Qiu, J. Duan, J. Garibaldi, and G. Qiu, "End-to-end fovea localisation in colour fundus images with a hierarchical deep regression network," *IEEE Transactions on Medical Imaging*, 2020.
- [15] S. Song, K. Dang, Q. Yu, Z. Wang, F. Coenen, J. Su, and X. Ding, "Bilateral-vit for robust fovea localization," in *2022 IEEE 19th International Symposium on Biomedical Imaging (ISBI)*. IEEE, 2022, pp. 1–5.
- [16] M. E. Gegundez-Arias, D. Marin, J. M. Bravo, and A. Suero, "Locating the fovea center position in digital fundus images using thresholding and feature extraction techniques," *Computerized Medical Imaging and Graphics*, 2013.
- [17] A. Giachetti, L. Ballerini, E. Trucco, and P. J. Wilson, "The use of radial symmetry to localize retinal landmarks," *Computerized Medical Imaging and Graphics*, 2013.
- [18] B. Dashtbozorg, J. Zhang, F. Huang, and B. M. ter Haar Romeny, "Automatic optic disc and fovea detection in retinal images using super-elliptical convergence index filters," in *International Conference on Image Analysis and Recognition*, 2016.
- [19] F. Girard, C. Kavalec, S. Grenier, H. B. Tahar, and F. Cheriet, "Simultaneous macula detection and optic disc boundary segmentation in retinal fundus images," in *Medical Imaging 2016: Image Processing*, 2016.
- [20] J. M. Molina-Casado, E. J. Carmona, and J. García-Feijó, "Fast detection of the main anatomical structures in digital retinal images based on intra-and inter-structure relational knowledge," *Computer methods and programs in biomedicine*, 2017.
- [21] S. Sedai, R. Tennakoon, P. Roy, K. Cao, and R. Garnavi, "Multi-stage segmentation of the fovea in retinal fundus images using fully convolutional neural networks," in *ISBI*, 2017.
- [22] B. Al-Bander, W. Al-Nuaimy, B. M. Williams, and Y. Zheng, "Multiscale sequential convolutional neural networks for simultaneous detection of fovea and optic disc," *Biomedical Signal Processing and Control*, 2018.
- [23] M. I. Meyer, A. Galdran, A. M. Mendonça, and A. Campilho, "A pixel-wise distance regression approach for joint retinal optical disc and fovea detection," in *MICCAI*, 2018.
- [24] Y. Huang, Z. Zhong, J. Yuan, and X. Tang, "Efficient and robust optic disc detection and fovea localization using region proposal network and cascaded network," *Biomedical Signal Processing and Control*, 2020.
- [25] B. J. Bhatkalkar, S. V. Nayak, S. V. Shenoy, and R. V. Arjunan, "Fundusposnet: A deep learning driven heatmap regression model for the joint localization of optic disc and fovea centers in color fundus images," *IEEE Access*, vol. 9, pp. 159 071–159 080, 2021.
- [26] A. Prakash, K. Chitta, and A. Geiger, "Multi-modal fusion transformer for end-to-end autonomous driving," in *Proceedings of the IEEE/CVF Conference on Computer Vision and Pattern Recognition*, 2021, pp. 7077–7087.
- [27] M. Ryoo, A. Piergiovanni, A. Arnab, M. Dehghani, and A. Angelova, "Tokenlearner: Adaptive space-time tokenization for videos," *Advances in Neural Information Processing Systems*, vol. 34, pp. 12 786–12 797, 2021.
- [28] Y. Fu, G. Zhang, J. Li, D. Pan, Y. Wang, and D. Zhang, "Fovea localization by blood vessel vector in abnormal fundus images," *Pattern Recognition*, vol. 129, p. 108711, 2022.
- [29] O. Ronneberger, P. Fischer, and T. Brox, "U-net: Convolutional networks for biomedical image segmentation," in *MICCAI*, 2015.
- [30] K. Suzuki, "Overview of deep learning in medical imaging," *Radiological physics and technology*, vol. 10, no. 3, pp. 257–273, 2017.
- [31] G. Murtaza, L. Shuib, A. W. Abdul Wahab, G. Mujtaba, H. F. Nweke, M. A. Al-garadi, F. Zulfiqar, G. Raza, and N. A. Azmi, "Deep learning-based breast cancer classification through medical imaging modalities: state of the art and research challenges," *Artificial Intelligence Review*, vol. 53, no. 3, pp. 1655–1720, 2020.
- [32] X. Qin, Z. Zhang, C. Huang, M. Dehghan, O. R. Zaiane, and M. Jagersand, "U2-net: Going deeper with nested u-structure for salient object detection," *Pattern Recognition*, vol. 106, 2020.
- [33] Q. Yu, K. Dang, N. Tajbakhsh, D. Terzopoulos, and X. Ding, "A location-sensitive local prototype network for few-shot medical image segmentation," in *ISBI*, 2021.
- [34] R. Yang and Y. Yu, "Artificial convolutional neural network in object detection and semantic segmentation for medical imaging analysis," *Frontiers in oncology*, vol. 11, p. 638182, 2021.
- [35] J. Cheng, L. Dong, and M. Lapata, "Long short-term memory-networks for machine reading," *arXiv preprint arXiv:1601.06733*, 2016.
- [36] H. Zhang, I. Goodfellow, D. Metaxas, and A. Odena, "Self-attention generative adversarial networks," in *International conference on machine learning*. PMLR, 2019, pp. 7354–7363.
- [37] J. H. Tan, U. R. Acharya, S. V. Bhandary, K. C. Chua, and S. Sivaprasad, "Segmentation of optic disc, fovea and retinal vasculature using a single convolutional neural network," *Journal of Computational Science*, vol. 20, pp. 70–79, 2017.
- [38] A. Vaswani, N. Shazeer, N. Parmar, J. Uszkoreit, L. Jones, A. N. Gomez, L. Kaiser, and I. Polosukhin, "Attention is all you need," *Advances in neural information processing systems*, vol. 30, 2017.
- [39] A. Dosovitskiy, L. Beyer, A. Kolesnikov, D. Weissenborn, X. Zhai, T. Unterthiner, M. Dehghani, M. Minderer, G. Heigold, S. Gelly *et al.*, "An image is worth 16x16 words: Transformers for image recognition at scale," *arXiv preprint arXiv:2010.11929*, 2020.
- [40] J. Chen, Y. Lu, Q. Yu, X. Luo, E. Adeli, Y. Wang, L. Lu, A. L. Yuille, and Y. Zhou, "Transunet: Transformers make strong encoders for medical image segmentation," *arXiv preprint arXiv:2102.04306*, 2021.
- [41] E. Decencière, X. Zhang, G. Cazuguel, B. Lay, B. Cochener, C. Trone, P. Gain, R. Ordonez, P. Massin, A. Erginay *et al.*, "Feedback on a publicly distributed image database: the messidor database," *Image Analysis & Stereology*, 2014.
- [42] H. Fu, F. Li, J. I. Orlando, H. Bogunovi, X. Sun, J. Liao, Y. Xu, S. Zhang, and X. Zhang, "Palm: Pathologic myopia challenge," 2019. [Online]. Available: <https://dx.doi.org/10.21227/55pk-8z03>
- [43] J. Staal, M. D. Abramoff, M. Niemeijer, M. A. Viergever, and B. Van Ginneken, "Ridge-based vessel segmentation in color images of the retina," *IEEE transactions on medical imaging*, 2004.
- [44] W. Wang, E. Xie, X. Li, D.-P. Fan, K. Song, D. Liang, T. Lu, P. Luo, and L. Shao, "Pyramid vision transformer: A versatile backbone for dense prediction without convolutions," in *Proceedings of the IEEE/CVF International Conference on Computer Vision*, 2021, pp. 568–578.
- [45] D. P. Kingma and J. Ba, "Adam: A method for stochastic optimization," *arXiv preprint arXiv:1412.6980*, 2014.
- [46] I. Sobh, L. Amin, S. Abdelkarim, K. Elmadawy, M. Saeed, O. Abdeltawab, M. Gamal, and A. El Sallab, "End-to-end multi-modal sensors fusion system for urban automated driving," 2018.